

Efficient Dual-domain Image Dehazing with Haze Prior Perception

Lirong Zheng, Yanshan Li, Rui Yu, Kaihao Zhang

Abstract—Transformer-based models exhibit strong global modeling capabilities in single-image dehazing, but their high computational cost limits real-time applicability. Existing methods predominantly rely on spatial-domain features to capture long-range dependencies, which are computationally expensive and often inadequate under complex haze conditions. While some approaches introduce frequency-domain cues, the weak coupling between spatial and frequency branches limits the overall performance. To overcome these limitations, we propose the Dark Channel Guided Frequency-aware Dehazing Network (DGFDNet), a novel dual-domain framework that performs physically guided degradation alignment across spatial and frequency domains. At its core, the DGFDNet block comprises two key modules: 1) the Haze-Aware Frequency Modulator (HAFM), which generates a pixel-level haze confidence map from dark channel priors to adaptively enhance haze-relevant frequency components, thereby achieving global degradation-aware spectral modulation; 2) the Multi-level Gating Aggregation Module (MGAM), which fuses multi-scale features through diverse convolutional kernels and hybrid gating mechanisms to recover fine structural details. Additionally, a Prior Correction Guidance Branch (PCGB) incorporates a closed-loop feedback mechanism, enabling iterative refinement of the prior by intermediate dehazed features and significantly improving haze localization accuracy, especially in challenging outdoor scenes. Extensive experiments on four benchmark haze datasets demonstrate that DGFDNet achieves state-of-the-art performance with superior robustness and real-time efficiency. Code is available at: <https://github.com/Dilizlr/DGFDNet>.

Index Terms—Image Dehazing, Frequency Learning, Dark-channel Guidance.

I. INTRODUCTION

IMAGES captured in hazy conditions often suffer from reduced contrast, weakened color saturation, and loss of high-frequency details. These degradations negatively affect downstream tasks such as object detection [1], [2] and semantic segmentation [3], [4]. Single-image dehazing aims to recover a clear scene from a hazy input. However, it remains a fundamentally ill-posed inverse problem due to the unknown and spatially varying distribution of haze.

Early methods [5]–[8] relied on handcrafted priors to estimate transmission maps and restore scene radiance. These methods are effective in simple scenes but often fail in complex real-world scenarios. With the rise of deep learning,

Lirong Zheng, Yanshan Li (corresponding author) and Rui Yu are with the Institute of Intelligent Information Processing, Guangdong Key Laboratory of Intelligent Information Processing, Shenzhen University, Shenzhen, China. E-mail: {zhenglirong2021@email.szu.edu.cn, lys@szu.edu.cn, yurui2020@email.szu.edu.cn}

Kaihao Zhang is with the School of Computer Science and Technology, Harbin Institute of Technology, Shenzhen, China. Email: {super.khzhang@gmail.com}

Manuscript received April 19, 2021; revised August 16, 2021.

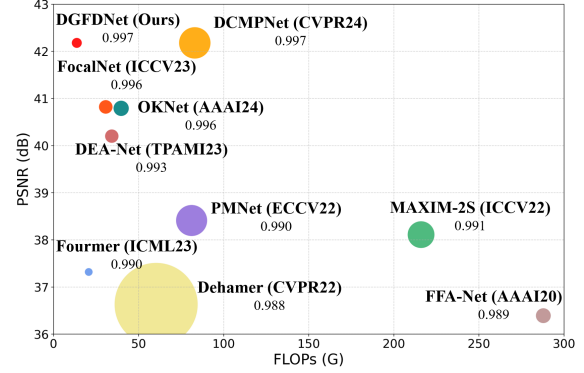


Fig. 1. Comparison results on the SOTS-Indoor dataset. The bubble size represents the number of model parameters, and the number below each model indicates the SSIM value.

CNN-based methods [9]–[12] have significantly improved reconstruction quality via end-to-end learning. However, their limited receptive fields restrict the modeling of global dependencies, which are crucial for restoring structural coherence and missing details. Recent Transformer-based architectures [13]–[15] have demonstrated strong capabilities in capturing long-range dependencies via self-attention mechanisms, further advancing dehazing performance. Yet, their quadratic complexity severely restricts their applicability in real-time scenarios.

To improve the efficiency of global context modeling, recent studies [16]–[19] have explored incorporating frequency-domain information into the dehazing process. This is motivated by the observation that haze mainly distorts the real and magnitude components of the Fourier spectrum, while the phase and imaginary parts largely preserve structural integrity (Fig. 2(a)). Moreover, local frequency alterations can induce global spatial effects (Fig. 2(b)), making frequency-based processing inherently more efficient for capturing long-range dependencies. However, existing spatial-frequency fusion methods typically employ loosely coupled dual-branch designs without explicit degradation alignment across domains. Such weak coupling limits effective information exchange and reduces robustness in complex haze scenarios.

To overcome these limitations, we propose the Dark Channel Guided Frequency-aware Dehazing Network (DGFDNet), a novel dual-domain framework that explicitly aligns haze degradation cues across spatial and frequency domains. By integrating haze localization in the spatial domain with targeted modulation in the frequency domain, DGFDNet effectively captures global context while maintaining computational

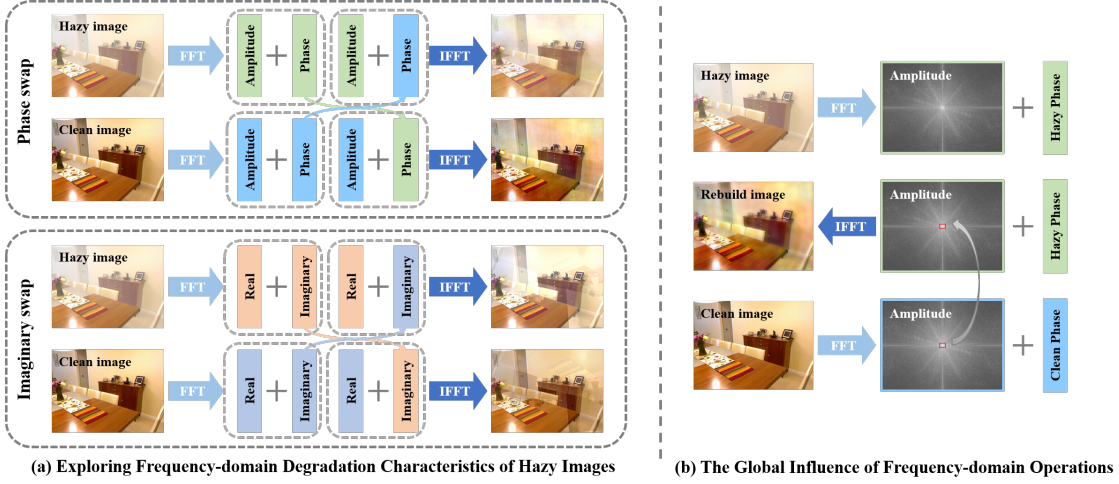


Fig. 2. (a) Investigation of the degradation characteristics of hazy images in the frequency domain by separately swapping the phase and imaginary components of hazy and clean images. (b) Demonstration of the global impact of frequency domain operations in the spatial domain by modifying local regions of the amplitude in hazy images.

efficiency, achieving a favorable balance between performance and practicality (see Fig. 1).

DGFDNet is composed of a cascade of multi-scale DGFD-Blocks, each containing two key modules: the Haze-Aware Frequency Modulator (HAFM) and the Multi-level Gating Aggregation Module (MGAM). HAFM generates a pixel-level haze confidence map using dark channel prior features for precise haze localization. Guided by this spatial prior, it adaptively modulates frequency-domain components to emphasize haze-relevant spectra while suppressing irrelevant information, thereby improving global degradation modeling and long-range context capture. MGAM focuses on local detail restoration by employing multi-scale convolutional kernels to capture diverse spatial patterns. Its core structure is a hybrid gating mechanism with hierarchical interaction that adaptively aggregates multi-scale features, enhancing reconstruction fidelity and fine-grained texture recovery.

Although the dark channel prior offers a coarse haze estimate, it often fails in complex outdoor scenes. To remedy this, we introduce the Prior Correction Guidance Branch (PCGB), which employs a closed-loop feedback mechanism to iteratively refine the prior using intermediate dehazed features. This progressive correction improves haze localization accuracy and significantly enhances the robustness and adaptability of the network under challenging real-world conditions.

By combining these components, each DGFDBlock jointly refines spatial and frequency-domain features, enhancing the robustness and effectiveness of DGFDNet. Our main contributions are summarized as follows:

1) We propose DGFDNet, a novel dual-domain dehazing framework that explicitly aligns degradation cues across spatial and frequency domains. Each DGFDBlock integrates HAFM for haze-aware frequency band modulation to model global context and MGAM for fine-grained detail restoration via adaptive multi-scale fusion.

2) We design PCGB, which employs a closed-loop feedback mechanism to iteratively refine the guidance of the dark

channel prior based on intermediate dehazed features. This dynamic correction significantly improves haze localization and model robustness in complex outdoor scenes.

3) Extensive experiments on both real-world and synthetic datasets demonstrate that DGFDNet achieves state-of-the-art dehazing performance while maintaining competitive computational efficiency.

II. RELATED WORK

A. Prior-based dehazing methods

Early dehazing approaches relied on handcrafted priors to constrain the solution space, typically derived from statistical analysis and empirical observations of natural images. Representative priors include the haze-line prior [20], color-line prior [21], dark channel prior (DCP) [5], color attenuation prior [6], and color ellipsoidal prior [8]. Among these, DCP is the most widely adopted. It assumes that in haze-free images, at least one color channel has near-zero intensity in most local patches, whereas haze increases this intensity, thereby enabling haze distribution estimation.

However, these priors often struggle in complex real-world scenes due to mismatches between their assumptions and actual conditions. For instance, DCP tends to fail in sky regions, where naturally low intensity contradicts its assumptions, resulting in notable transmission estimation errors.

B. CNNs-based dehazing methods

CNN-based methods leverage deep convolutions to learn features from large-scale data, offering greater adaptability than handcrafted priors. Early models such as DehazeNet [9], AOD-Net [22], and MSCNN [23] laid the foundation for CNN-based dehazing. Subsequent works integrated attention mechanisms to enhance feature representation, including Grid-DehazeNet [24] with multi-scale fusion and FFA-Net [25] with pixel and channel attention. HFMCA-Net [26] further improves multi-scale feature learning through hierarchical

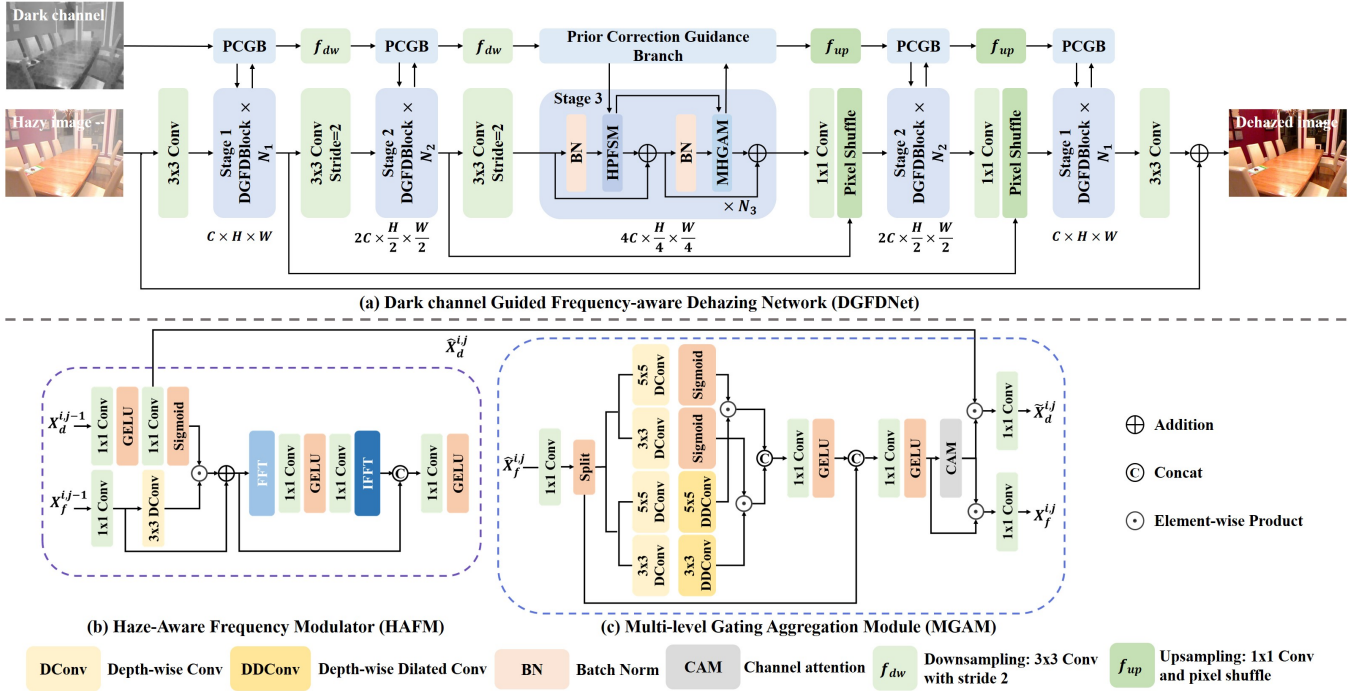


Fig. 3. Overview of DGFDNet. (a) It includes a Dehazing Main Branch and Prior Correction Guidance Branch (PCGB), both with a three-scale symmetric design and inter-stage information exchange. The core module, DGFDBlock, The core module, DGFDBlock, incorporates (b) HAFM for global context modeling and (c) MGAM for local information modeling.

fusion and mixed convolution attention, while more recent approaches such as TFFD-Net [27] and DEA-Net [28] focus on fine detail recovery through task-specific modules.

Despite their success, CNNs still struggle to model long-range dependencies due to limited receptive fields. Deepening the network can help, but it increases computational cost and latency, limiting real-time deployment.

C. Transformer-based dehazing methods

Transformers [29]–[34] have attracted significant attention in image restoration tasks for their strong global modeling capabilities, including dehazing. Dehazer [35] is among the first to refine local CNN features using Transformer-based global representations. DehazeFormer [14] adapts the Swin Transformer with task-specific designs, while STH [36] adopts a multi-branch architecture to handle varying haze densities. DehazeDCT [37] integrates deformable convolutions to better address spatially variant haze, and MB-TaylorFormer V2 [38] introduces a Taylor series-inspired approximation to reduce Transformer complexity.

While Transformer-based models excel at capturing long-range dependencies, they suffer from two major limitations: quadratic complexity that grows with image resolution, and difficulty in restoring fine-grained local details essential for high-quality reconstruction.

D. Frequency-domain dehazing methods

Recent studies have explored frequency-domain techniques for single-image dehazing. Nehete et al. [16] propose a two-stage network that processes amplitude and phase separately.

WSAMF-Net [39] integrates spatial and frequency features using a wavelet-based spatial attention module. Cui et al. [40] introduce a dual-domain selection mechanism to extract key features from both domains. However, they only suppress low-frequency components without global spectral modulation, and their spatial attention fails to accurately localize degraded regions. Yu et al. [17] propose a dual-guided framework to fuse spatial and frequency cues, but their amplitude-driven phase reconstruction may propagate errors when amplitude features are corrupted.

These methods demonstrate the promise of frequency-aware restoration. However, most of them rely on shallow fusion strategies with loosely coupled dual-branch designs. They lack explicit alignment of degradation information across domains, which limits the integration of complementary features.

III. METHOD

As shown in Fig. 3 (a), DGFDNet consists of a dehazing main branch and a prior correction guidance branch. The main branch adopts a U-shaped encoder-decoder with three symmetric stages, each containing multiple DGFDBlocks. The number of blocks and channels varies across stages to handle different resolutions. Strided convolution enables downsampling, while upsampling combines 1×1 convolution and pixel shuffle. Skip connections facilitate feature transfer between encoder and decoder stages. The guidance branch extracts haze-related features from the dark channel prior to assist HAFM in haze perception and receives feedback from MGAM for dynamic refinement. It follows the same downsampling and upsampling structure as the main branch to ensure consistency.

Given a hazy image $I \in \mathbb{R}^{3 \times H \times W}$, a 3×3 convolution extracts shallow features $X_f \in \mathbb{R}^{C \times H \times W}$, while the dark channel prior is computed using [5]. The shallow features and dark channel prior are fed into the main and guidance branches, respectively, which interact bidirectionally to generate restored features. A final 3×3 convolution maps these features back to the image space, producing a residual image $I_r \in \mathbb{R}^{3 \times H \times W}$. The dehazed output is then obtained as $I_c = I + I_r$.

A. Haze-Aware Frequency Modulator

1) *Motivation*: The spectral characteristics of haze degradation (Fig. 2) suggest that frequency-domain processing is more effective than spatial-domain methods in separating haze from background content. However, its inherent global modulation reduces sensitivity to subtle degradations, which can distort fine details. To solve this, many methods [16], [17] adopt dual-branch architectures that process spatial and frequency domains separately before fusing information via interaction modules. But the loose coupling often limits effective information exchange and fails to fully leverage the complementary strengths of both domains.

In contrast, the proposed HAFM alternates processing between spatial and frequency domains to maximize their synergy while maintaining efficiency. It first focuses on haze-affected regions in the spatial domain to extract structural priors that guide frequency-domain restoration. Specifically, we use the dark channel guidance to generate a spatial attention map that more accurately localizes degraded areas and quantifies their severity than traditional spatial attention. Crucially, this attention mechanism inherently modulates haze-related frequency bands, enabling frequency-domain processing to rapidly capture haze features and perform precise modulation. Such explicit alignment of degradation cues strengthens global modeling and preserves fine details for high-quality restoration.

2) *Pipeline*: Given the input feature $X_f^{i,j-1}$ and the dark channel-guided feature $X_d^{i,j-1}$ for the j -th DGFDBlock at the i -th stage, the HAFM processing can be formulated as:

$$\hat{X}_f^{i,j}, \hat{X}_d^{i,j} = X_f^{i,j-1} + \text{HAFM}(\text{BN}(X_f^{i,j-1}), X_d^{i,j-1}), \quad (1)$$

where BN represents Batch Norm, $\hat{X}_f^{i,j}$ is the residual output feature of HAFM, and $\hat{X}_d^{i,j}$ is the intermediate dark channel-guided feature.

Spatial Modulation. As illustrated in Fig. 3(b), HAFM first performs spatial modulation. The dark channel-guided feature $X_d^{i,j-1}$ is passed through two consecutive 1×1 convolutions with a GELU activation in between, producing the intermediate dark channel feature $\hat{X}_d^{i,j}$. Both convolutions serve to compress channels. Then, $\hat{X}_d^{i,j}$ is processed with a Sigmoid function to produce the spatial attention map M_{sa} . This process is expressed as:

$$\hat{X}_d^{i,j} = \text{Conv}_{1 \times 1}(\text{GELU}(\text{Conv}_{1 \times 1}(X_d^{i,j-1}))), \quad (2)$$

$$M_{sa} = \text{Sigmoid}(\hat{X}_d^{i,j}). \quad (3)$$

Meanwhile, the normalized input feature $\text{BN}(X_f^{i,j-1})$ is processed by a 1×1 convolution to produce $X_m^{i,j}$, for inter-channel

information exchange. To recover high-frequency details lost in hazy regions, a 3×3 depth-wise convolution is applied to $X_m^{i,j}$. The result is then element-wise multiplied by the dark channel-guided spatial attention map M_{sa} and added to $X_m^{i,j}$, yielding the final spatially modulated feature:

$$X_{spatial}^{i,j} = \text{DConv}_{3 \times 3}(X_m^{i,j}) \odot M_{sa} + X_m^{i,j}. \quad (4)$$

Frequency Modulation. Global frequency modulation is then applied to the spatially modulated feature $X_{spatial}^{i,j}$. First, the feature undergoes a Fast Fourier Transform (FFT, \mathcal{F}) to obtain its real and imaginary components, $X_{\mathcal{R}}^{i,j}$ and $X_{\mathcal{I}}^{i,j}$. Each part is processed independently using two 1×1 convolutions with a GELU activation in between, functioning like a frequency-domain MLP. This design preserves spectral structure while avoiding cross-component interference. Then, the modulated parts are transformed back to the spatial domain via the inverse FFT (IFFT, \mathcal{F}^{-1}), yielding the frequency-modulated feature $X_{frequency}^{i,j}$. The entire process is formulated as:

$$X_{\mathcal{R}}^{i,j}, X_{\mathcal{I}}^{i,j} = \mathcal{F}(X_{spatial}^{i,j}), \quad (5)$$

$$\hat{X}_{\mathcal{R}}^{i,j}, \hat{X}_{\mathcal{I}}^{i,j} = \text{Conv}_{1 \times 1}(\text{GELU}(\text{Conv}_{1 \times 1}(X_{\mathcal{R}}^{i,j}, \hat{X}_{\mathcal{I}}^{i,j}))), \quad (6)$$

$$X_{frequency}^{i,j} = \mathcal{F}^{-1}(\hat{X}_{\mathcal{R}}^{i,j}, \hat{X}_{\mathcal{I}}^{i,j}). \quad (7)$$

Finally, the spatially and frequency-modulated features are concatenated along the channel dimension and subsequently fused using a 1×1 convolution followed by a GELU activation to generate the final output:

$$X^{i,j} = \text{GELU}(\text{Conv}_{1 \times 1}(\text{Cat}(X_{spatial}^{i,j}, X_{frequency}^{i,j}))). \quad (8)$$

B. Multi-level Gating Aggregation Module

1) *Motivation*: Global modeling ensures structural consistency, while local modeling restores fine textures essential for high-quality recovery. Some Transformer-based methods [41], [42] enhance local perception using single-scale depth-wise convolutions, but often neglect multi-scale feature learning, which is crucial for handling uneven haze.

To tackle this, we propose MGAM, which enhances local modeling through multi-scale feature extraction. By stacking small-kernel convolutions, MGAM captures multi-level representations and expands the receptive field at low computational cost. Unlike DSANet [43], which uses parallel large-kernel convolutions, our approach extracts features across different scales more efficiently. Here, “level” borrows the convention from U-Net, referring to receptive field size rather than spatial resolution.

Moreover, we introduce a hybrid gating mechanism that leverages low-level features rich in edge and texture cues to regulate the propagation of high-level semantic information. This modulation enables hierarchical interaction, facilitating adaptive feature fusion while preserving fine details. Additionally, the sensitivity of low-level features to local haze variations enhances the model’s ability to maintain semantic consistency and robustness under non-uniform haze conditions.

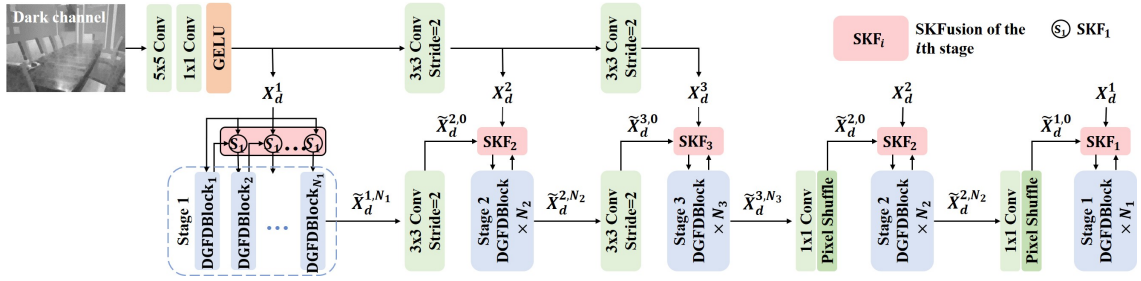


Fig. 4. The detailed structure of PCGB. PCGB follows the three-scale design of the dehazing main branch, progressively fusing original and feedback dark channel features through SKFusion, which is shared across all DGFBBlocks at each stage.

2) *Pipeline*: Given the output feature $\hat{X}_f^{i,j}$ of HAFM and the intermediate dark channel-guided feature $\hat{X}_d^{i,j}$, the processing flow of MGAM is defined as:

$$X_f^{i,j}, \hat{X}_d^{i,j} = \hat{X}_f^{i,j} + \text{MGAM}(\text{BN}(\hat{X}_f^{i,j}), \hat{X}_d^{i,j}), \quad (9)$$

where $X_f^{i,j}$ denotes the residual output feature of MGAM, and $\hat{X}_d^{i,j}$ is the dark channel correction feature.

In MGAM, we first apply a 1×1 convolution to the input feature (after BN) to double the number of channels. As shown in Fig. 3 (c), the resulting feature is split into two parts: one for extracting multi-scale features $X_{fea}^{i,j}$, and the other for generating gating signals $X_{gate}^{i,j}$. This process is expressed as:

$$X_{fea}^{i,j}, X_{gate}^{i,j} = \text{Split}(\text{Conv}_{1 \times 1}(\text{BN}(\hat{X}_f^{i,j}))). \quad (10)$$

Multi-scale Feature Extraction. Each of the two parallel branches applies two stacked depth-wise convolutions for multi-scale feature extraction. The first convolution in each branch uses $k \times k$ kernels, while the second uses the same kernels with a dilation factor of 2 to expand the receptive field. The process is defined as follows:

$$X_{fea_k}^{i,j} = \text{DDConv}_{k \times k}(\text{DConv}_{k \times k}(X_{fea}^{i,j})), \quad k \in \{3, 5\}, \quad (11)$$

where $X_{fea_k}^{i,j}$ represents the output feature of the $k \times k$ branch.

Gating Signals Generation. A dual-branch structure generates gating signals, where each branch applies a depth-wise convolution with $k \times k$ kernels and a Sigmoid activation:

$$X_{gate_k}^{i,j} = \text{Sigmoid}(\text{DConv}_{k \times k}(X_{gate}^{i,j})), \quad k \in \{3, 5\}, \quad (12)$$

where $X_{gate_k}^{i,j}$ represents the gating signal corresponding to the $k \times k$ feature branch.

Multi-scale Feature Fusion. The gated features are obtained via element-wise multiplication of $X_{fea_k}^{i,j}$ and $X_{gate_k}^{i,j}$:

$$X_{gated_k}^{i,j} = X_{fea_k}^{i,j} \odot X_{gate_k}^{i,j}, \quad k \in \{3, 5\}. \quad (13)$$

These features are concatenated and processed by a 1×1 convolution with GELU activation, producing the fusion feature $X_{dual}^{i,j}$. To mitigate early-stage gating instability, a skip connection incorporates the original input feature before a final 1×1 convolution and GELU activation, yielding the multi-scale fusion feature $X_{mult}^{i,j}$. The entire process is formulated as follows:

$$X_{dual}^{i,j} = \text{GELU}(\text{Conv}_{1 \times 1}(\text{Cat}(X_{gated_3}^{i,j}, X_{gated_5}^{i,j}))), \quad (14)$$

$$X_{mult}^{i,j} = \text{GELU}(\text{Conv}_{1 \times 1}(\text{Cat}(\text{BN}(\hat{X}_f^{i,j}), X_{dual}^{i,j}))). \quad (15)$$

Feature Feedback Module. A Channel Attention Module [44] (CAM) is applied at the end of MGAM to generate feedback for PCGB while reducing redundancy in multi-scale feature extraction. The attention map M_{ca} is computed from $X_{mult}^{i,j}$ and applied element-wise to both $X_{mult}^{i,j}$ and $\hat{X}_d^{i,j}$:

$$X_f^{i,j} = \text{Conv}_{1 \times 1}(X_{mult}^{i,j} \odot M_{ca}), \quad (16)$$

$$\hat{X}_d^{i,j} = \text{Conv}_{1 \times 1}(\hat{X}_d^{i,j} \odot M_{ca}), \quad (17)$$

where $X_f^{i,j}$ represents the final output and $\hat{X}_d^{i,j}$ is the feedback dark channel correction feature. This operation enables PCGB to utilize the information of $X_{mult}^{i,j}$ while selectively emphasizing important channels, enhancing its connection with the dehazing branch.

C. Prior Correction Guidance Branch

1) *Motivation*: Although the dark channel prior provides a rough estimation of haze distribution, it often fails in outdoor scenes containing sky regions. Its assumption of locally uniform haze does not hold in real-world scenarios with complex backgrounds and varying haze densities, limiting its effectiveness for accurate haze localization.

Still, physically grounded priors provide useful inductive bias, which helps models generalize better to unseen conditions. For instance, Dehamer [35] incorporates the dark channel prior into positional encodings to enhance haze perception. However, it treats the prior as static and lacks correction during inference, which may lead to suboptimal guidance when the prior is inaccurate.

To address this, we propose the Prior Correction Guidance Branch (PCGB). Instead of using the dark channel prior as a fixed input, PCGB treats it as a haze-awareness cue and progressively refines the guidance features through feedback from the main dehazing branch. This design preserves the benefits of inductive bias while improving haze localization under complex and non-uniform conditions.

2) *Pipeline*: As illustrated in Fig. 4, given the dark channel $X_d \in \mathbb{R}^{H \times W}$ of the hazy image I , we first encode the features using two successive convolutional layers:

$$X_d^1 = \text{GELU}(\text{Conv}_{1 \times 1}(\text{Conv}_{5 \times 5}(X_d))), \quad (18)$$

where $X_d^1 \in \mathbb{R}^{C \times H \times W}$ denotes the initial dark channel feature of the first stage. Then, downsampling is performed to derive the initial dark channel features for the second and third stages:

$$X_d^i = f_{dw}(X_d^{i-1}), \quad i \in \{2, 3\} \quad (19)$$

where X_d^i denotes the initial dark channel feature for the i -th stage, and f_{dw} denotes downsampling, which halves the spatial resolution while doubling the channel number.

Dark Channel-Guided Features in the Encoder. The first DGFDBlock in the first stage uses X_d^1 as the dark channel-guided feature, denoted as $X_d^{1,0} = X_d^1$. In later stages, the first DGFDBlock obtains its dark channel-guided feature by downsampling the feedback dark channel correction from the last DGFDBlock of the previous stage and fusing it with the initial dark channel feature of the current stage via SKFusion [14]. For subsequent DGFDBlocks within a stage, the feedback dark channel correction from the previous DGFDBlock is directly fused with the initial dark channel feature. The process is expressed as:

$$X_d^{i,j-1} = \begin{cases} X_d^1, & i = 1, j = 1 \\ \text{SKF}_i(\tilde{X}_d^{i,j-1}, X_d^i), & 1 < j \leq N_i \\ \text{SKF}_i(f_{dw}(\tilde{X}_d^{i-1, N_{i-1}}), X_d^i). & i > 1, j = 1 \end{cases} \quad (20)$$

Here, $X_d^{i,j-1}$ represents the dark channel-guided feature for the j -th DGFDBlock at the i -th stage in the encoder. N_{i-1} is the number of DGFDBlocks in the previous stage, and $\tilde{X}_d^{i,j-1}$ denotes the feedback dark channel correction from the preceding DGFDBlock. SKF_i is the SKFusion [14] block shared across all DGFDBlocks within the i -th stage. The downsampling operation f_{dw} maintains parameter consistency with the one used for initial dark channel features.

Dark Channel-Guided Features in the Decoder. The decoder follows a reversed process, propagating from Stage 3 back to Stage 1. Unlike the encoder, the first DGFDBlock in each stage obtains its dark channel-guided feature by upsampling the feedback dark channel correction from the last DGFDBlock of the previous stage and fusing it with the initial dark channel feature of the current stage via SKFusion [14]:

$$X_d^{i,j-1} = \begin{cases} \text{SKF}_i(f_{up}(\tilde{X}_d^{i+1, N_{i+1}}), X_d^i), & j = 1 \\ \text{SKF}_i(\tilde{X}_d^{i,j-1}, X_d^i). & 1 < j \leq N_i \end{cases} \quad (21)$$

Here, $X_d^{i,j-1}$ is the dark channel-guided feature for the j -th DGFDBlock at the i -th stage in the decoder. N_{i+1} denotes the number of DGFDBlocks in the next stage, and f_{up} is an upsampling operation combining a 1×1 convolution with pixel-shuffle, doubling the spatial dimensions and halving the channel number.

D. Loss Function

To simultaneously improve detail recovery and global structure restoration, we adopt a dual-domain L_1 loss that supervises both spatial and frequency domains. This encourages the network to balance fine-grained texture reconstruction with consistent global appearance. The overall loss is defined as:

$$\mathcal{L} = \|I_c - I_g\|_1 + \lambda \|\mathcal{F}(I_c) - \mathcal{F}(I_g)\|_1, \quad (22)$$

where I_c is the dehazed output of DGFDNet, I_g is the ground-truth image, \mathcal{F} denotes the Fast Fourier Transform, and λ is a balancing parameter that controls the contribution of the frequency domain loss. In our experiments, λ is set to 0.1.

TABLE I
DETAILED TRAINING CONFIGURATION OF DIFFERENT EVALUATION DATASETS.

Evaluation dataset	Init lr	Batch size	Patch size	Epochs
SOTS-Indoor	3e-4	8	256×256	1000
SOTS-Outdoor	1e-4	8	256×256	60
Dense-Haze	2e-4	2	512×512	5000
NH-HAZE	3e-4	4	384×384	6000

IV. EXPERIMENTS

A. Experimental settings

Datasets. We evaluate the proposed DGFDNet on both synthetic and real-world datasets. The synthetic dataset is the RESIDE [45] dataset, which includes two training sets: the ITS with 13,990 indoor image pairs and the OTS with 313,950 outdoor image pairs. The test set SOTS consists of 500 indoor and 500 outdoor image pairs. For real-world datasets, we use Dense-Haze [46] and NH-HAZE [47], each containing 55 paired real images. The last five pairs of each dataset are used for testing, and the rest for training.

Comparison settings. We compare DGFDNet with ten CNN-based methods: GridDehazeNet [24], MSBDN [48], FFA-Net [25], PMNet [49], MAXIM-2S [50], DEA-Net [28], FocalNet [40], OKNet [51], PGH2Net [52], and DCMPNet [53]. We further include three Transformer-based models: DeHamer [35], DehazeFormer [14], and Fourmer [54]. All methods are evaluated using Peak Signal-to-Noise Ratio (PSNR) and Structural Similarity Index Measure (SSIM).

Training details. Each stage of the model contains 2, 2, 4, 2, 2 DGFDBlocks, with a base channel size of 32. We use the Adam optimizer with $\beta_1 = 0.9$ and $\beta_2 = 0.999$. The initial learning rate is dataset-dependent and is gradually reduced to 1×10^{-6} following a cosine annealing schedule (Table I). Data augmentation includes random cropping and flipping. FLOPs are calculated on 256×256 image patches. All experiments are conducted on an NVIDIA 3090 GPU.

B. Comparison with State-of-the-art Methods

1) Quantitative Comparisons: Table II presents quantitative comparisons between DGFDNet and state-of-the-art methods on two synthetic and two real-world datasets. Bold and underlined values indicate the best and second-best results, respectively. Overall, our method outperforms all existing approaches across all datasets.

Compared to classical CNN-based methods like FocalNet [40] and OKNet [51], DGFDNet improves PSNR by 1.36 dB and 1.39 dB on SOTS-Indoor, and by 0.80 dB and 0.83 dB on SOTS-Outdoor, while using roughly half the parameters and less than half the FLOPs. Unlike FocalNet, which also adopts dual-domain selection mechanism with spatial attention, our method integrates dark channel-guided attention for more precise haze localization and a full-frequency modulation unit to better handle varying degradation levels.

Compared to the heavy DCMPNet [53], DGFDNet achieves comparable results on SOTS-Indoor with only 12.0% of its parameters and 19.7% of its FLOPs. On SOTS-Outdoor,

TABLE II
QUANTITATIVE COMPARISONS WITH STATE-OF-THE-ART DEHAZING METHODS ON THE SYNTHETIC AND REAL-WORLD DATASETS.

Method	Venue & Year	SOTS-Indoor		SOTS-Outdoor		Dense-Haze		NH-HAZE		Overhead	
		PSNR	SSIM	PSNR	SSIM	PSNR	SSIM	PSNR	SSIM	Params	FLOPs
GridDehazeNet [24]	ICCV 2019	32.16	0.984	30.86	0.982	13.31	0.37	13.80	0.54	0.956M	21.49G
MSBDN [48]	CVPR 2020	33.67	0.985	33.48	0.982	15.37	0.49	19.23	0.71	31.35M	41.54G
FFA-Net [25]	AAAI 2020	36.39	0.989	33.57	0.984	14.39	0.45	19.87	0.69	4.456M	287.8G
PMNet [49]	ECCV 2022	38.41	0.990	34.74	0.985	16.79	0.51	20.42	0.73	18.90M	81.13G
MAXIM-2S [50]	ICCV 2022	38.11	0.991	34.19	0.985	-	-	-	-	14.10M	216.0G
Dehamer [35]	CVPR 2022	36.63	0.988	35.18	0.986	16.62	0.56	20.66	0.68	132.50M	60.3G
Fourmer [54]	ICML 2023	37.32	0.990	-	-	15.95	0.49	-	-	1.29M	20.6G
DehazeFormer [14]	TIP 2023	40.05	<u>0.996</u>	34.29	0.983	-	-	19.11	0.66	4.634M	48.64G
FocalNet [40]	ICCV 2023	40.82	<u>0.996</u>	<u>37.71</u>	0.995	<u>17.07</u>	0.63	20.43	0.79	3.74M	30.63G
DEA-Net [28]	TIP 2024	40.20	0.993	36.03	0.989	-	-	-	-	3.65M	34.19G
OKNet [51]	AAAI 2024	40.79	<u>0.996</u>	37.68	0.995	16.92	<u>0.64</u>	20.48	<u>0.80</u>	4.72M	39.71G
DCMPNet [53]	CVPR 2024	42.18	0.997	36.56	<u>0.993</u>	-	-	-	-	17.36M	69.23G
PGH2Net [52]	AAAI 2025	41.70	0.996	37.52	0.989	17.02	0.61	-	-	1.76M	16.05G
DGFNet (Ours)	-	42.18	0.997	38.51	0.995	18.34	0.67	<u>20.49</u>	0.81	2.08M	13.65G

DGFNet surpasses DCMPNet by 1.95 dB PSNR and 0.002 SSIM, demonstrating enhanced robustness in complex outdoor conditions. This improvement mainly arises from the PCGB module, which effectively mitigates the limitations of traditional dark channel priors.

Under similar resource budgets, DGFNet consistently outperforms the lightweight PGH2Net [52], achieving 0.48 dB higher PSNR on SOTS-Indoor and 0.99 dB PSNR plus 0.006 SSIM gains on SOTS-Outdoor, indicating a superior trade-off between accuracy and efficiency.

Beyond synthetic datasets, our method performs exceptionally well on real-world datasets, including Dense-Haze [46] and NH-HAZE [47]. While its PSNR on NH-HAZE is slightly lower than Dehamer [35], it ranks second overall. Notably, it achieves the highest SSIM on both datasets, demonstrating its strong generalization and ability to reconstruct global structures in real-world hazy scenarios.

2) *Qualitative Comparisons*: Fig.5 shows dehazing results on synthetic images from the SOTS dataset. Our method consistently achieves the highest PSNR across all testing images. In the first row of Fig. 5(b, c), FFA-Net [25] and MAXIM-2S [50] produce blurred edges and noticeable artifacts in complex indoor scene. Additionally, MAXIM-2S [50] and Dehamer [35] exhibit insufficient haze removal in deeper regions, as shown in the second row of Fig. 5(c, d). While FocalNet [40] and OKNet [51] perform better, our method still surpasses them. As shown in Fig. 5(f), our approach not only removes haze more effectively but also preserves sharp edges, delivering superior visual quality. In outdoor scenes, our method continues to outperform others, achieving more thorough haze removal and clearer reconstruction.

Fig.6 and Fig.7 show real-world dehazing results on Dense-Haze [46] and NH-HAZE [47] datasets. In Fig.6, two dense haze scenes are compared. In the first scene, our method achieves slightly lower PSNR than Dehamer [35] but surpasses it by 0.183 in SSIM, delivering clearer textures and reduced color distortion. The second scene features severe haze with

significant detail loss. Even in this challenging case, our method better restores the overall structure of the image and preserves more details compared to Dehamer [35].

Fig. 7 compares two non-homogeneous haze scenes. Except for a slightly lower PSNR in the second scene compared to FocalNet [40], our method leads on all other metrics. In the first scene, our dehazing result exhibits minimal color distortion and avoids the heavy artifacts introduced by other methods. In the second scene, our method removes haze most thoroughly, revealing the clearest details, though it also mistakenly removes some snow traces on the ground.

Overall, our method achieves the highest SSIM across all real-world cases, demonstrating strong global structure recovery even under severe haze-induced detail degradation.

C. Ablation Studies

We first evaluate the individual and combined contributions of HAFM, MGAM, and PCGB to verify their effectiveness and complementarity. Next, we perform ablation studies by modifying each module independently while keeping the rest of the architecture fixed. All models are trained on the ITS dataset and evaluated on SOTS-Indoor under the same conditions as the final model. Since PCGB targets the limitations of dark channel priors in outdoor scenes, we additionally validate its performance on SOTS-Outdoor using a model trained on the OTS dataset. Finally, attention map visualizations are used to demonstrate the corrective effect of PCGB.

1) *Effectiveness of Core Modules*: To thoroughly evaluate the effectiveness and complementarity of the three core modules, we design four variants: MGAM, HAFM (without feedback correction), HAFM+PCGB (with complete feedback-guided correction), and MGAM+HAFM. Table III summarizes the performance of each variant.

As shown in Table III, MGAM improves PSNR by 0.75 dB over HAFM with the same SSIM of 0.994, highlighting its advantage in local detail enhancement. Introducing PCGB into HAFM yields an additional 0.70 dB gain, demonstrating

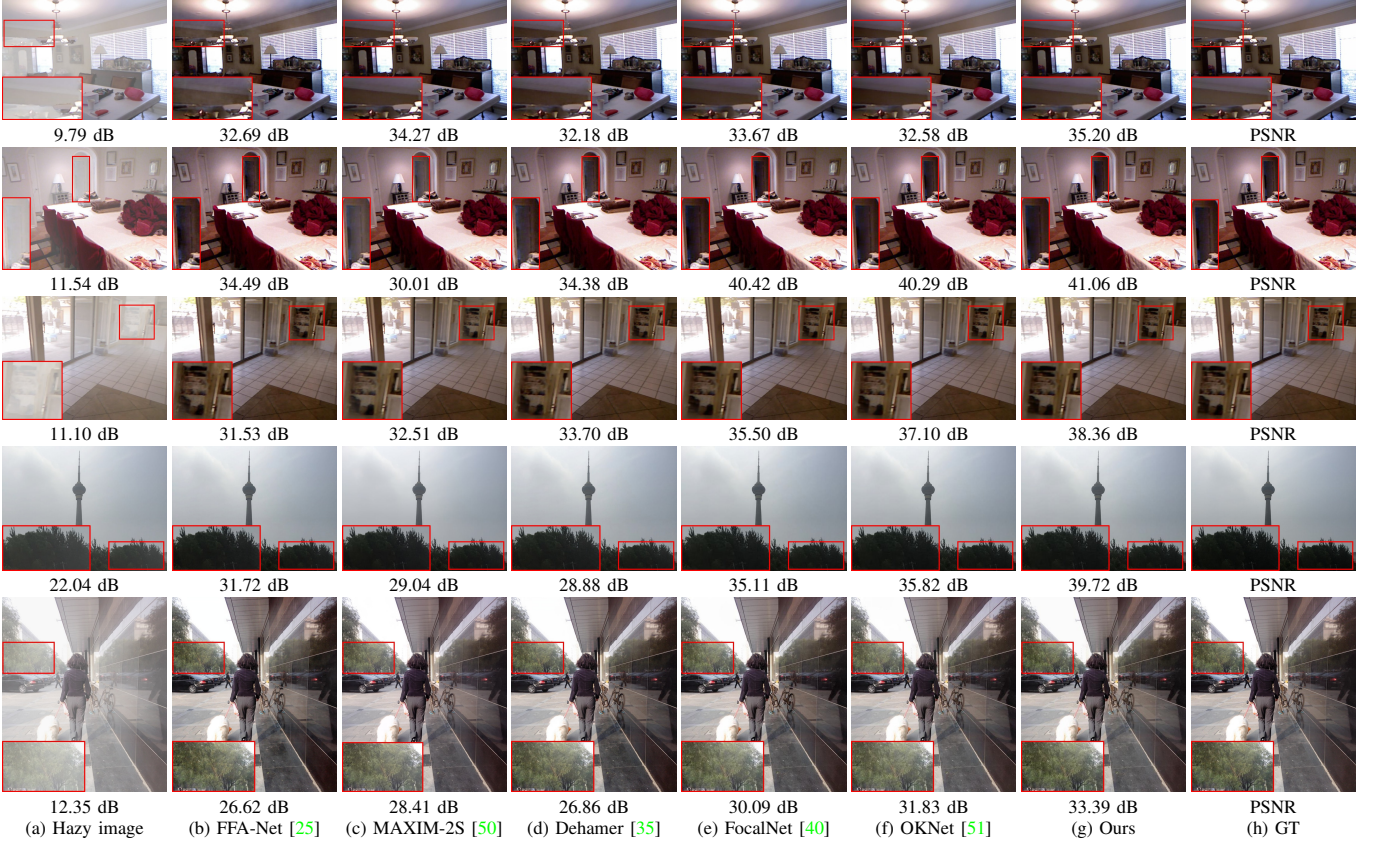


Fig. 5. Visual comparisons on synthetic hazy images from the SOTS dataset. Key regions highlighted by red boxes are enlarged and placed in the lower-left corner of each image for clearer comparison.

TABLE III
ABLATION STUDY FOR THREE CORE MODULES.

Variant	SOTS-Indoor		Overhead	
	PSNR	SSIM	Params	FLOPs
MGAM	40.10	0.994	0.88M	8.39G
HAFM	39.35	0.994	1.12M	4.69G
HAFM+PCGB	40.05	0.995	1.48M	7.26G
MGAM+HAFM	41.90	0.996	2.03M	11.94G
Full Network	42.18	0.997	2.08M	13.65G

its role in enhancing global degradation modeling through adaptive prior correction. Combining MGAM and HAFM brings a substantial PSNR increase of 1.80 dB over MGAM alone and 2.55 dB over HAFM. This gain benefits from the synergy between multi-scale spatial feature extraction and dual-domain modulation. Further adding PCGB achieves the best overall result, confirming that the three modules are complementary and jointly contribute to both local and global restoration. These improvements are achieved with minimal additional computational cost.

2) *Effectiveness of HAFM*: To validate HAFM, we design four variants: HAFM-S (spatial modulation only), HAFM-F (frequency modulation only), HAFM-SSA (standard spatial attention replacing dark channel-guided attention), and HAFM-SMLP (spatial MLP replacing frequency modulation). The results are exhibited in Table IV.

TABLE IV
ABLATION STUDY FOR KEY COMPONENTS IN HAFM.

Variant	SOTS-Indoor		Overhead	
	PSNR	SSIM	Params	FLOPs
HAFM-S	41.12	0.996	1.31M	12.78G
HAFM-F	41.18	0.996	1.83M	10.95G
HAFM-SSA	41.78	0.996	1.84M	11.13G
HAFM-SMLP	41.91	0.997	2.09M	20.22G
Full HAFM	42.18	0.997	2.08M	13.65G

According to Table IV, using only spatial (HAFM-S) or only frequency modulation (HAFM-F) leads to PSNR drops of 1.06 dB and 1.00 dB, respectively, compared to the full HAFM. This highlights the necessity of combining both spatial and frequency modulation for optimal performance. When dark channel-guided attention is replaced with standard spatial attention (HAFM-SSA), PSNR decreases by 0.40 dB, and SSIM drops by 0.001. This confirms that dark channel-guided attention provides more effective haze localization than its conventional counterpart. Furthermore, replacing the frequency-domain MLP with a spatial MLP (HAFM-SMLP) results in a 48.1% increase in FLOPs, yet PSNR remains 0.27 dB lower than the full HAFM. This demonstrates that frequency-domain processing not only improves computational efficiency but also enhances global feature modeling.

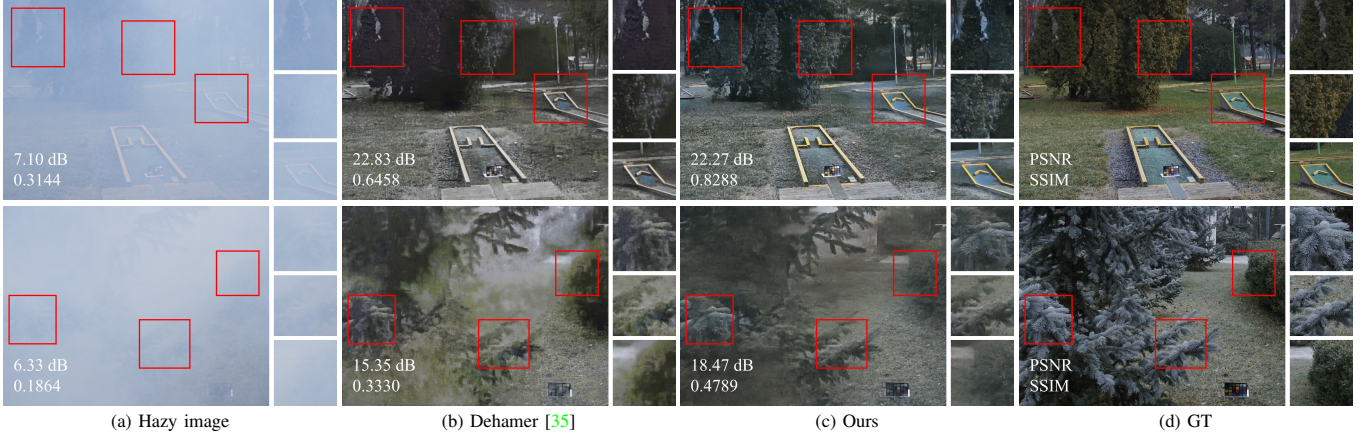


Fig. 6. Visual comparisons on real-world hazy images from the Dense-Haze datasets. Key regions marked with red boxes are enlarged in left-to-right order and arranged vertically on the right.



Fig. 7. Visual comparisons on real-world hazy images from the NH-Haze dataset. Key regions marked with red boxes are enlarged in left-to-right order and arranged horizontally at the bottom.

TABLE V
ABLATION STUDY FOR KEY COMPONENTS IN MGAM.

Variant	SOTS-Indoor		Overhead	
	PSNR	SSIM	Params	FLOPs
MGAM-3 × 3	41.79	0.995	1.93M	11.74G
MGAM-5 × 5	41.58	0.996	1.97M	12.45G
MGAM-Nogate	41.15	0.996	1.97M	12.34G
MGAM-Noskip	41.76	0.996	1.91M	12.01G
Full MGAM	42.18	0.997	2.08M	13.65G

3) *Effectiveness of MGAM*: To assess the contribution of each MGAM component, we conduct an ablation study with four variants: MGAM-3 × 3 (only the 3 × 3 gated branch), MGAM-5 × 5 (only the 5 × 5 gated branch), MGAM-Nogate (both branches without gating), and MGAM-Noskip (removing the skip connection). The results are reported in Table V.

From the results, MGAM-3 × 3 achieves 0.21 dB higher

PSNR but 0.001 lower SSIM compared to MGAM-5 × 5. This indicates that small-kernel convolutions are more sensitive to local texture recovery, whereas large-kernel convolutions are better at capturing global structural information. By integrating both branches, the full MGAM balances these strengths, yielding simultaneous improvements in PSNR and SSIM.

Removing the gating mechanism while retaining the dual-branch structure (MGAM-Nogate) causes PSNR and SSIM to drop by 1.03 dB and 0.001, respectively, highlighting the importance of dynamic gating. By allowing low-level features to regulate the flow of high-level information, the gating mechanism enhances adaptive feature selection and helps mitigate detail loss in deeper layers. Additionally, removing the skip connection from the original input (MGAM-Noskip) results in a PSNR decrease of 0.42 dB and an SSIM decrease of 0.001, underscoring the importance of the skip connection in correcting selection bias introduced by the gating mechanism.

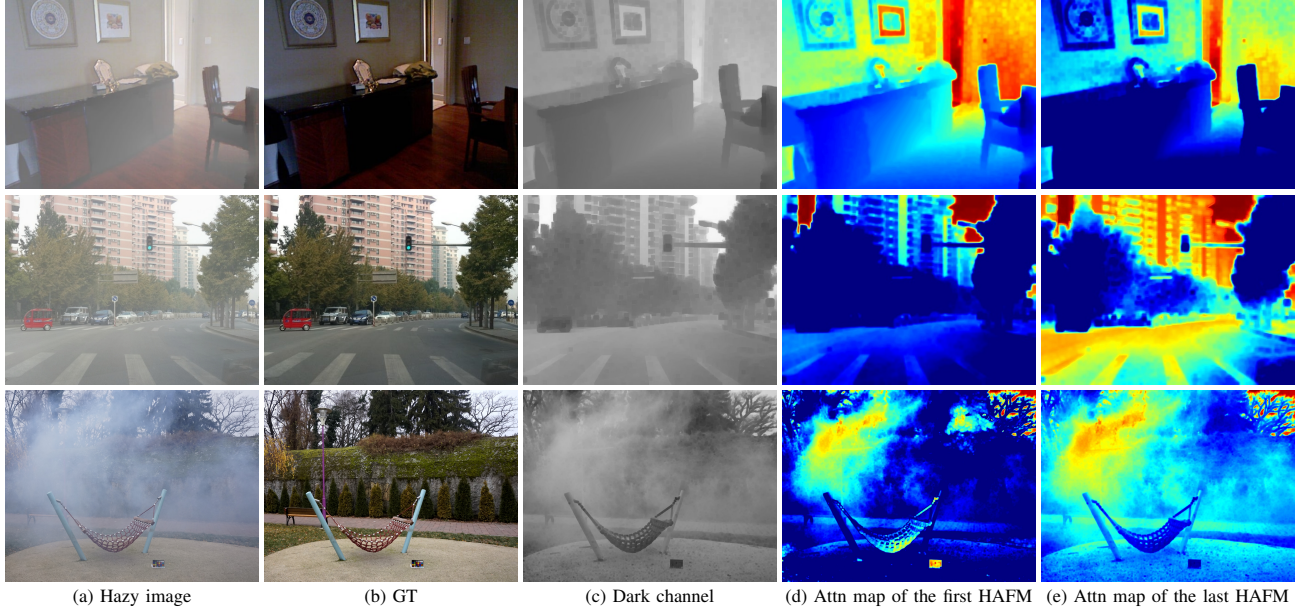


Fig. 8. Visual study of PCGB for dehazing. From left to right: hazy images, ground truth images, dark channels of the hazy images, and dark channel-guided spatial attention maps generated by the first and last HAFM.

TABLE VI
ABLATION STUDY FOR KEY COMPONENTS IN PCGB ON SOTS-INDOOR.

Variant	SOTS-Indoor		Overhead	
	PSNR	SSIM	Params	FLOPs
PCGB-SSA	41.78	0.996	1.84M	11.13G
PCGB-NoFR	41.90	0.996	2.03M	11.94G
PCGB-DAF	42.02	0.996	2.07M	13.62G
PCGB-PFF	41.47	0.996	2.08M	13.05G
Full PCGB	42.18	0.997	2.08M	13.65G

TABLE VII
ABLATION STUDY FOR KEY COMPONENTS IN PCGB ON SOTS-OUTDOOR.

Variant	SOTS-Outdoor		Overhead	
	PSNR	SSIM	Params	FLOPs
PCGB-SSA	37.81	0.995	1.84M	11.13G
PCGB-NoFR	37.53	0.994	2.03M	11.94G
PCGB-DAF	37.95	0.995	2.07M	13.62G
PCGB-PFF	37.82	0.995	2.08M	13.05G
Full PCGB	38.51	0.995	2.08M	13.65G

4) *Effectiveness of PCGB*: To validate the rationale behind PCGB, we implement four variants: (1) PCGB-SSA replaces dark channel-guided spatial attention with standard spatial attention, the same as HAFM-SSA; (2) PCGB-NoFR generates the spatial attention map using only the initial dark channel features, without feedback refinement; (3) PCGB-DAF directly adds feedback correction features to the initial dark channel features instead of using SKFusion [14]; (4) PCGB-PFF uses the initial prior only in the first DGFDBlock, while subsequent blocks fuse the previous guidance with correction features via SKFusion. Table VI and Table VII present the results on SOTS-Indoor and SOTS-outdoor datasets, respectively.

Indoor results. Results in Table VI indicate that the dark channel prior is relatively reliable in indoor scenes, making it an effective guidance cue. Even without feedback refinement, PCGB-NoFR outperforms PCGB-SSA by 0.12 dB in PSNR, validating the prior’s ability to localize haze and estimate degradation. Introducing feedback correction via simple addition (PCGB-DAF) brings a further 0.12 dB gain, while replacing addition with SKFusion in the full PCGB improves PSNR and SSIM by 0.16 dB and 0.001, respectively, showing enhanced adaptability to structural complexity. However, PCGB-PFF, which discards the prior after the first block, leads to a 0.71 dB PSNR drop, suggesting that consistent use of the initial prior across layers is important for stable and accurate guidance indoors.

Outdoor results. In contrast, the dark channel prior becomes less reliable in outdoor environments due to factors such as sky and bright regions. As shown in Table VII, PCGB-NoFR performs 0.28 dB worse than PCGB-SSA, highlighting the limitations of the prior alone. Introducing feedback correction (PCGB-DAF) compensates for this, achieving gains of 0.42 dB over PCGB-NoFR and 0.14 dB over PCGB-SSA. PCGB-PFF, which progressively fuses the prior with feedback features, also improves over NoFR by 0.29 dB and performs comparably to PCGB-SSA, suggesting that reducing reliance on noisy priors is beneficial outdoors. Nevertheless, PCGB-DAF still outperforms PCGB-PFF by 0.13 dB, indicating that retaining some contribution from the initial prior remains helpful. The full PCGB achieves the best performance, surpassing PCGB-DAF by 0.56 dB, confirming that SKFusion effectively handles the diverse and non-uniform haze patterns typical of outdoor scenes.

5) *Visual Analysis of PCGB*: To further evaluate the corrective effect of PCGB, we visualize the dark channel-guided spatial attention maps from the first and last HAFM modules

of DGFDNet. The visualization covers three representative scenes from the SOTS-Indoor, SOTS-Outdoor, and NH-HAZE datasets, as shown in Fig. 8.

In the indoor scene, the initial attention map closely reflects the raw dark channel distribution, resulting in widespread activation across the image. After feedback refinement, the attention becomes more concentrated on heavily degraded areas, improving both the accuracy of haze localization and the effectiveness of spatial modulation.

In contrast, the outdoor scene reveals the limitations of dark channel priors. Due to low dark channel values in bright areas such as the sky, the initial attention map tends to overemphasize these regions while neglecting genuinely hazy areas like distant buildings and road surfaces. Through feedback refinement, PCGB progressively redirects attention away from the sky and toward the actual degradation, narrowing the response gap and mitigating over-processing. This leads to more balanced and accurate spatial attention.

Under complex real-world degradations, PCGB exhibits even stronger corrective capabilities. In the NH-HAZE example, the initial attention map mistakenly activates on irrelevant structures such as the swing's mesh, resulting in false positives. Moreover, it primarily focuses on dense haze areas while neglecting mildly degraded regions, leading to insufficient coverage. After iterative refinement, the final attention map more accurately aligns with the actual haze distribution. It effectively suppresses false activations and enhances sensitivity to previously neglected regions. These results confirm the robustness of PCGB in handling spatially diverse and challenging degradation patterns.

V. CONCLUSION

In this paper, we propose DGFDNet, a dual-domain dehazing framework that explicitly aligns spatial and frequency-domain degradation cues under dark channel guidance. To address the inefficiency and weak coupling in existing spatial-frequency models, DGFDNet introduces three key modules: the Haze-Aware Frequency Modulator (HAFM) for degradation-aware spectral filtering, the Multi-level Gating Aggregation Module (MGAM) for adaptive multi-scale spatial feature fusion, and the Prior Correction Guidance Branch (PCGB) for iterative refinement of dark channel priors. These modules form a compact and computationally efficient framework that effectively captures long-range dependencies while preserving fine details, robustly handling both homogeneous and non-homogeneous haze distributions. Extensive experiments on both synthetic and real-world dehazing benchmarks demonstrate that DGFDNet achieves superior dehazing performance with strong generalization and computational efficiency, making it well-suited for practical deployment.

ACKNOWLEDGMENTS

This work was partially supported by National Natural Science Foundation of China (Nos.62471317), Natural Science Foundation of Shenzhen (No. JCYJ20240813141331042), and Guangdong Provincial Key Laboratory (Grant 2023B1212060076).

REFERENCES

- [1] Z. Chen, H. Ji, Y. Zhang, Z. Zhu, and Y. Li, "High-resolution feature pyramid network for small object detection on drone view," *IEEE Transactions on Circuits and Systems for Video Technology*, vol. 34, no. 1, pp. 475–489, 2024.
- [2] Y. Shi, S. Zhao, J. Wu, Z. Wu, and H. Yan, "Fixated object detection based on saliency prior in traffic scenes," *IEEE Transactions on Circuits and Systems for Video Technology*, vol. 34, no. 3, pp. 1413–1426, 2024.
- [3] J. Yang, L. Bai, Y. Sun, C. Tian, M. Mao, and G. Wang, "Pixel difference convolutional network for rgb-d semantic segmentation," *IEEE Transactions on Circuits and Systems for Video Technology*, vol. 34, no. 3, pp. 1481–1492, 2024.
- [4] X. Shi, Z. Yin, G. Han, W. Liu, L. Qin, Y. Bi, and S. Li, "Bssnet: A real-time semantic segmentation network for road scenes inspired from autoencoder," *IEEE Transactions on Circuits and Systems for Video Technology*, vol. 34, no. 5, pp. 3424–3438, 2024.
- [5] K. He, J. Sun, and X. Tang, "Single image haze removal using dark channel prior," *IEEE Transactions on Pattern Analysis and Machine Intelligence*, vol. 33, no. 12, pp. 2341–2353, 2011.
- [6] Q. Zhu, J. Mai, and L. Shao, "A fast single image haze removal algorithm using color attenuation prior," *IEEE Transactions on Image Processing*, vol. 24, no. 11, pp. 3522–3533, 2015.
- [7] J. Wang, K. Lu, J. Xue, N. He, and L. Shao, "Single image dehazing based on the physical model and msrccr algorithm," *IEEE Transactions on Circuits and Systems for Video Technology*, vol. 28, no. 9, pp. 2190–2199, 2018.
- [8] T. M. Bui and W. Kim, "Single image dehazing using color ellipsoid prior," *IEEE Transactions on Image Processing*, vol. 27, no. 2, pp. 999–1009, 2018.
- [9] B. Cai, X. Xu, K. Jia, C. Qing, and D. Tao, "Dehazenet: An end-to-end system for single image haze removal," *IEEE Transactions on Image Processing*, vol. 25, no. 11, pp. 5187–5198, 2016.
- [10] L. Lu, Q. Xiong, B. Xu, and D. Chu, "Mixdehazenet: Mix structure block for image dehazing network," in *2024 International Joint Conference on Neural Networks (IJCNN)*, 2024, pp. 1–10.
- [11] L. Zheng, Y. Li, K. Zhang, and W. Luo, "T-net: Deep stacked scale-iteration network for image dehazing," *IEEE Transactions on Multimedia*, vol. 25, pp. 6794–6807, 2023.
- [12] T. Wang, G. Tao, W. Lu, K. Zhang, W. Luo, X. Zhang, and T. Lu, "Restoring vision in hazy weather with hierarchical contrastive learning," *Pattern Recogn.*, vol. 145, no. C, Jan. 2024. [Online]. Available: <https://doi.org/10.1016/j.patcog.2023.109956>
- [13] Y. Liu, J. Li, Y. Ma, Q. Xie, and Y. Liu, "Hcanet: Haze-concentration-aware network for real-scene dehazing with codebook priors," in *Proceedings of the 32nd ACM International Conference on Multimedia*, ser. MM '24. New York, NY, USA: Association for Computing Machinery, 2024, p. 9136–9144. [Online]. Available: <https://doi.org/10.1145/3664647.3681314>
- [14] Y. Song, Z. He, H. Qian, and X. Du, "Vision transformers for single image dehazing," *IEEE Transactions on Image Processing*, vol. 32, pp. 1927–1941, 2023.
- [15] Y. Yang, H. Zhang, X. Wu, and X. Liang, "Mstfdn: Multi-scale transformer fusion dehazing network," *Applied Intelligence*, vol. 53, no. 5, pp. 5951–5962, Mar 2023. [Online]. Available: <https://doi.org/10.1007/s10489-022-03674-2>
- [16] H. Nehete, A. Monga, P. Kaushik, and B. K. Kaushik, "Fourier prior-based two-stage architecture for image restoration," in *2024 IEEE/CVF Conference on Computer Vision and Pattern Recognition Workshops (CVPRW)*, 2024, pp. 6014–6023.
- [17] Y. Cui, Q. Wang, C. Li, W. Ren, and A. Knoll, "Eenet: An effective and efficient network for single image dehazing," *Pattern Recognition*, vol. 158, p. 111074, 2025.
- [18] H. Yu, N. Zheng, M. Zhou, J. Huang, Z. Xiao, and F. Zhao, "Frequency and spatial dual guidance for image dehazing," in *Computer Vision – ECCV 2022*, S. Avidan, G. Brostow, M. Cissé, G. M. Farinella, and T. Hassner, Eds. Cham: Springer Nature Switzerland, 2022, pp. 181–198.
- [19] L. Wang, H. Dong, R. Li, C. Zhu, H. Tao, Y. Guo, and F. Wang, "Dual-path dehazing network with spatial-frequency feature fusion," *Pattern Recognition*, vol. 151, p. 110397, 2024. [Online]. Available: <https://www.sciencedirect.com/science/article/pii/S0031320324001481>
- [20] D. Berman, T. treibitz, and S. Avidan, "Non-local image dehazing," in *Proceedings of the IEEE Conference on Computer Vision and Pattern Recognition (CVPR)*, June 2016.
- [21] R. Fattal, "Dehazing using color-lines," *ACM Trans. Graph.*, vol. 34, no. 1, Dec. 2015.

[22] B. Li, X. Peng, Z. Wang, J. Xu, and D. Feng, "Aod-net: All-in-one dehazing network," in *2017 IEEE International Conference on Computer Vision (ICCV)*, 2017, pp. 4780–4788.

[23] W. Ren, S. Liu, H. Zhang, J. Pan, X. Cao, and M. H. Yang, "Single image dehazing via multi-scale convolutional neural networks," in *Computer Vision – ECCV 2016*, 2016, pp. 154–169.

[24] X. Liu, Y. Ma, Z. Shi, and J. Chen, "Griddehazenet: Attention-based multi-scale network for image dehazing," in *Proceedings of the IEEE/CVF International Conference on Computer Vision (ICCV)*, October 2019.

[25] X. Qin, Z. Wang, Y. Bai, X. Xie, and H. Jia, "Ffa-net: Feature fusion attention network for single image dehazing," in *Proceedings of the AAAI Conference on Artificial Intelligence*, vol. 34, no. 07, 2020, pp. 11 908–11 915.

[26] X. Zhang, J. Wang, T. Wang, and R. Jiang, "Hierarchical feature fusion with mixed convolution attention for single image dehazing," *IEEE Transactions on Circuits and Systems for Video Technology*, vol. 32, no. 2, pp. 510–522, 2022.

[27] C. Li, W. Yan, H. Zhao, S. Zhou, and Y. Wang, "Tffd-net: an effective two-stage mixed feature fusion and detail recovery dehazing network," *The Visual Computer*, Oct 2024. [Online]. Available: <https://doi.org/10.1007/s00371-024-03642-6>

[28] Z. Chen, Z. He, and Z.-M. Lu, "Dea-net: Single image dehazing based on detail-enhanced convolution and content-guided attention," *IEEE Transactions on Image Processing*, vol. 33, pp. 1002–1015, 2024.

[29] R. Zhu, Z. Tu, J. Liu, A. C. Bovik, and Y. Fan, "Mwformer: Multi-weather image restoration using degradation-aware transformers," *IEEE Transactions on Image Processing*, vol. 33, pp. 6790–6805, 2024.

[30] J. M. J. Valanarasu, R. Yasarla, and V. M. Patel, "Transweather: Transformer-based restoration of images degraded by adverse weather conditions," in *Proceedings of the IEEE/CVF Conference on Computer Vision and Pattern Recognition (CVPR)*, June 2022, pp. 2353–2363.

[31] L. Liu, S. Yuan, J. Liu, X. Guo, Y. Yan, and Q. Tian, "Siamtrans: Zero-shot multi-frame image restoration with pre-trained siamese transformers," *Proceedings of the AAAI Conference on Artificial Intelligence*, vol. 36, no. 2, pp. 1747–1755, Jun. 2022. [Online]. Available: <https://ojs.aaai.org/index.php/AAAI/article/view/20067>

[32] T. Wang, K. Zhang, Z. Shao, W. Luo, B. Stenger, T. Lu, T.-K. Kim, W. Liu, and H. Li, "Gridformer: Residual dense transformer with grid structure for image restoration in adverse weather conditions," *International Journal of Computer Vision*, vol. 132, no. 10, pp. 4541–4563, 2024.

[33] S. Zhou, D. Chen, J. Pan, J. Shi, and J. Yang, "Adapt or perish: Adaptive sparse transformer with attentive feature refinement for image restoration," in *Proceedings of the IEEE/CVF Conference on Computer Vision and Pattern Recognition*, 2024, pp. 2952–2963.

[34] X. Chen, H. Li, M. Li, and J. Pan, "Learning a sparse transformer network for effective image deraining," in *2023 IEEE/CVF Conference on Computer Vision and Pattern Recognition (CVPR)*, 2023, pp. 5896–5905.

[35] C. Guo, Q. Yan, S. Anwar, R. Cong, W. Ren, and C. Li, "Image dehazing transformer with transmission-aware 3d position embedding," in *2022 IEEE/CVF Conference on Computer Vision and Pattern Recognition (CVPR)*, 2022, pp. 5802–5810.

[36] J. Wu, Z. Liu, F. Huang, and R. Luo, "Adaptive haze pixel intensity perception transformer structure for image dehazing networks," *Scientific Reports*, vol. 14, no. 1, p. 22435, 2024.

[37] W. Dong, H. Zhou, R. Wang, X. Liu, G. Zhai, and J. Chen, "Dehazedct: Towards effective non-homogeneous dehazing via deformable convolutional transformer," in *2024 IEEE/CVF Conference on Computer Vision and Pattern Recognition Workshops (CVPRW)*, 2024, pp. 6405–6414.

[38] Z. Jin, Y. Qiu, K. Zhang, H. Li, and W. Luo, "Mb-taylorformer v2: improved multi-branch linear transformer expanded by taylor formula for image restoration," *IEEE Transactions on Pattern Analysis and Machine Intelligence*, 2025.

[39] X. Song, D. Zhou, W. Li, H. Ding, Y. Dai, and L. Zhang, "Wsamf-net: Wavelet spatial attention-based multistream feedback network for single image dehazing," *IEEE Transactions on Circuits and Systems for Video Technology*, vol. 33, no. 2, pp. 575–588, 2023.

[40] Y. Cui, W. Ren, X. Cao, and A. Knoll, "Focal network for image restoration," in *2023 IEEE/CVF International Conference on Computer Vision (ICCV)*, 2023, pp. 12 955–12 965.

[41] Z. Wang, X. Cun, J. Bao, W. Zhou, J. Liu, and H. Li, "Uformer: A general u-shaped transformer for image restoration," in *2022 IEEE/CVF Conference on Computer Vision and Pattern Recognition (CVPR)*, 2022, pp. 17 662–17 672.

[42] S. W. Zamir, A. Arora, S. Khan, M. Hayat, F. S. Khan, and M.-H. Yang, "Restormer: Efficient transformer for high-resolution image restoration," in *Proceedings of the IEEE/CVF Conference on Computer Vision and Pattern Recognition (CVPR)*, June 2022, pp. 5728–5739.

[43] Y. Cui and A. Knoll, "Dual-domain strip attention for image restoration," *Neural Networks*, vol. 171, pp. 429–439, 2024.

[44] Y. Zhang, K. Li, K. Li, L. Wang, B. Zhong, and Y. Fu, "Image super-resolution using very deep residual channel attention networks," in *Proceedings of the European conference on computer vision (ECCV)*, 2018, pp. 286–301.

[45] B. Li, W. Ren, D. Fu, D. Feng, W. Zeng, and Z. Wang, "Benchmarking single-image dehazing and beyond," *IEEE Transactions on Image Processing*, vol. 28, no. 1, pp. 492–505, 2018.

[46] C. O. Ancuti, C. Ancuti, M. Sbert, and R. Timofte, "Dense-haze: A benchmark for image dehazing with dense-haze and haze-free images," in *2019 IEEE international conference on image processing (ICIP)*. IEEE, 2019, pp. 1014–1018.

[47] C. O. Ancuti, C. Ancuti, and R. Timofte, "Nh-haze: An image dehazing benchmark with non-homogeneous hazy and haze-free images," in *2020 IEEE/CVF Conference on Computer Vision and Pattern Recognition Workshops (CVPRW)*, 2020, pp. 1798–1805.

[48] H. Dong, J. Pan, L. Xiang, Z. Hu, X. Zhang, F. Wang, and M.-H. Yang, "Multi-scale boosted dehazing network with dense feature fusion," in *Proceedings of the IEEE/CVF conference on computer vision and pattern recognition*, 2020, pp. 2157–2167.

[49] T. Ye, Y. Zhang, M. Jiang, L. Chen, Y. Liu, S. Chen, and E. Chen, "Perceiving and modeling density for image dehazing," in *European conference on computer vision*. Springer, 2022, pp. 130–145.

[50] Z. Tu, H. Talebi, H. Zhang, F. Yang, P. Milanfar, A. Bovik, and Y. Li, "Maxim: Multi-axis mlp for image processing," in *Proceedings of the IEEE/CVF conference on computer vision and pattern recognition*, 2022, pp. 5769–5780.

[51] Y. Cui, W. Ren, and A. Knoll, "Omni-kernel network for image restoration," in *Proceedings of the AAAI conference on artificial intelligence*, vol. 38, no. 2, 2024, pp. 1426–1434.

[52] X. Su, S. Li, Y. Cui, M. Cao, Y. Zhang, Z. Chen, Z. Wu, Z. Wang, Y. Zhang, and X. Yuan, "Prior-guided hierarchical harmonization network for efficient image dehazing," in *Proceedings of the AAAI Conference on Artificial Intelligence*, vol. 39, no. 7, 2025, pp. 7042–7050.

[53] Y. Zhang, S. Zhou, and H. Li, "Depth information assisted collaborative mutual promotion network for single image dehazing," in *Proceedings of the IEEE/CVF Conference on Computer Vision and Pattern Recognition (CVPR)*, June 2024, pp. 2846–2855.

[54] M. Zhou, J. Huang, C.-L. Guo, and C. Li, "Fourmer: An efficient global modeling paradigm for image restoration," in *International conference on machine learning*. PMLR, 2023, pp. 42 589–42 601.